Spatial Interpolation of Cyclostationary Test Statistics in Cognitive Radio Networks: Methods and Field Measurements

S. Chaudhari, *Member, IEEE,* M. Kosunen, *Member, IEEE,* S. Mäkinen, C. Ramanathan, J. Oksanen, *Student Member, IEEE,* M. Laatta, *Student Member, IEEE,* J. Ryynänen, *Member, IEEE* V. Koivunen, *Fellow, IEEE,* and M. Valkama, *Senior Member, IEEE,*

***Abstract*—The focus of this paper is on evaluating different spatial interpolation methods for the construction of radio environment map (REM) using field measurements obtained by cyclostationary based mobile sensors. Mobile sensing devices employing cyclostationary detectors provide lot of advantages compared to widely-used energy detectors such as robustness to noise uncertainty and ability to distinguish among different primary user signals. However, mobile sensing results are not available at locations between the sensors making it difficult for a secondary user (possibly without a spectrum sensor) to decide whether to use primary user resources at that location. To overcome this, spatial interpolation of test statistics measured at limited number of locations can be carried out to create a channel occupancy map at unmeasured locations between the sensors. For this purpose, different spatial interpolation techniques for the cyclostationary test statistic have been employed in this paper such as inverse distance weighting (IDW), ordinary Kriging (OK), and universal Kriging (UK). The effectiveness of these methods is demonstrated by applying them on extensive real-world field measurement data obtained by mobile-phone-compliant spectrum sensors. The field measurements were carried out using four mobile spectrum sensors measuring eight DVB-T channels at more than hundred locations encompassing roughly one-third of the area of the city of Espoo in Finland. The accuracy of the spatial interpolation results based on the field measurements is determined using the cross-validation approach with the widely-used root mean square error (RMSE) as the metric. Field measurement results indicate that reliable results with spatial coverage can be achieved using Kriging for cyclostationary based test statistics. Comparison of spatial interpolation results of cyclostationary test statistics is also carried out with those of energy values obtained during the measurement campaign in the form of received signal strength indicator (RSSI). Comparison results clearly show the performance improvement and robustness obtained using cyclostationary based detectors instead of energy detectors.**

***Index Terms*—Cognitive radio, cyclostationary detection, energy detection, Kriging, radio environment map, spatial estimation, spectrum sensing.**

I. Introduction

Realization of the opportunistic spectrum usage in cognitive radio networks requires spectrum awareness in the form of radio environment map (REM). REM, which is also called *spectrum cartography*, tells us the status of available radios in a given region along with their locations, assigned frequency bands, coverage areas, and interference levels [1]. REMs can also be used, for example, to construct potential fields for routing [2] and scheduling [3] purposes. REM can be constructed from database of transmitters or through field measurements acquired by sensors [1]. Databases generally rely on deterministic or empirical propagation models to construct REM while spectrum sensing based solutions use actual field measurements and spatial interpolation techniques. Details of database-based REM implementation can be found in [4], [5] while details about measurements-based REM implementation can be found in [1], [6].

In this paper, we consider REM construction based on field measurements as they provide several benefits over the database based approaches. REM constructed through the field measurements are more accurate as the differences between the assumed and actual propagation conditions may result in errors in the REM constructed using a database [7]. Although real-world field measurements require hardware, this is not a severe problem in the world of ubiquitous communication as the required hardware can be implemented efficiently even in mobile devices [8]. A detailed quantitative complexity-comparison of the two REM construction methods is difficult as complexity in these two spectral awareness techniques arise from different requirements [9]. For example, spectrum sensing entails higher transceiver complexity while the database solution leads to higher infrastructure complexity [10]. Since exact quantitative comparison is difficult, only qualitative comparison is possible and has been carried out in [5], [10]. Moreover, construction of REM through database and field measurements are not mutually exclusive but can complement each other and allow for improving the accuracy of the REM. For example, details regarding how measurements aid the database are given in [11], [12] while it was concluded in [13] that a database assisted spectrum sensing may present the most efficient solution for secondary access in the radar frequencies.

In general, it is not feasible to measure the parameters at every location in the area of interest. Even large scale wireless sensor networks are known to suffer from coverage holes that may result from demanding propagation environments (e.g., tall buildings or hilly terrain), hardware failures, data corruption, extensive costs of redeployment or the hostility of deployment areas [14]. Simply using the closest measurement

This research has been carried out as a part of the "Enabling Methods for Dynamic Spectrum Access and Cognitive Radio" project within the TRIAL technology programme funded by TEKES (The Finnish Funding Agency for Technology and Innovation). Research of S. Chaudhari and C. Ramanathan was partially supported by the Science and Engineering Research Board, India under grant no. ECR/2015/000010.

point does not necessarily give the best approximation regarding the channel occupancy in a complex radio environment. The coverage issues can be mitigated by the means of *spatial interpolation*, also called as *spatial prediction*, which refers to estimating the parameter values at unmeasured locations using known values at the measured locations. In the context of spatial interpolation, the 'unmeasured locations' or 'unsampled locations' in this paper represent the locations between the measured locations where the secondary user does not have sensing capability.

Spatial interpolation methods can be divided into deterministic and statistical variants. In deterministic methods, the weights used in the interpolation estimates do not depend on the observed data but only on the geometry of the measurement locations. Examples of the deterministic methods are *Thiessen or Voronoi polygons*, and *inverse distance weighting (IDW)* interpolation, as well as *trend surfaces* and *splines* [15], [16]. One example of statistical methods is *Kriging*, which is a generic name for a family of generalized least-squares regression algorithms, used in recognition of the pioneering work of Danie Krige [16]. It is a statistical interpolation technique where statistics of the spatial data are considered for interpolation. There are several benefits from using Kriging compared to the deterministic alternatives [14], [16]. First, Kriging can extrapolate the data outside the measurement hull. Second, in addition to the interpolation estimates, Kriging also provides estimates for the interpolation variance quantifying the reliability of the interpolated value. This helps in evaluating the feasibility of using the method for spectrum sensing purposes with noisy or otherwise unreliable data.

Current literature [6], [14], [17] mainly focuses on the interpolation of energy estimates which are well handled with majority of the traditional interpolation methods combined with radio wave propagation models. However, a well-known problem with energy detection is that it cannot distinguish between the signals of interest and interference. Furthermore, its performance is heavily affected by hardware non-idealities such as nonlinearity and noise uncertainty causing an effect known as the SNR wall [18]. Thus, in consumer-grade hardware, the energy detector can only be used to obtain coarse estimates on the field strength. As opposed to energy detectors, cyclostationary feature detectors have higher sensitivity and are robust against noise and interference [19], [20]. However, no studies or experiments have been carried out for the spatial interpolation of cyclostationary statistics in the current literature. Cyclostationary based sensing statistics depend on spatial processes such as radio propagation which are stochastic in nature. There is often a good general understanding about their spatial correlation structure. Deterministic methods do not allow using information about such statistical spatial variation. Kriging on the other hand makes use of this understanding. Motivated by this, our paper focuses on evaluating the performance of deterministic as well as statistical interpolation methods while using cyclostationary based field measurements.

The contributions of this paper are the following:

- The field measurement campaign was carried out in eight DVB-T channels (channel numbers 42-49 corresponding to 642-698 MHz center frequency range) with 8 MHz bandwidth each. The measurements were carried out at more than 100 different locations in the city of Espoo in Finland using four distinct mobile measurement set-ups covering close to 200 km^2. At each location, 400 cyclostationary test statistics and RSSI values were collected.
- The cyclostationary test statistic utilized in this paper is Angular Domain spatial sign correlation Detector Test (ADDT), which was originally proposed in [8] and is implemented using FPGA technology.
- An analytical expression is derived for the distribution of the ADDT statistic under noise-only hypothesis. This helps in finding the threshold of a Neyman-Pearson detector.
- Performance evaluation of different spatial interpolation techniques such as IDW, ordinary kriging (OK) and universal kriging (UK) is done for the cyclostationary test statistic computed from real-world measurement data. Different fitting variograms are experimented with including circular, spherical, exponential, Gaussian, and stable models.
- Effect of the number of nearest measured locations (or nearest neighbors) is also studied on the estimation of the test statistic at a given unmeasured location. This is important as the complexity of the algorithm and its accuracy depend on the effect of number of nearest neighbors.
- Spatial interpolation is also carried out for energy detection test (EDT) statistics and its performance is compared to the results of cyclostationary based interpolation results.

The current work differs from our previous work [7], [21] in that the current work is based on new large-scale field measurements conducted using a different implementation of cyclostationary detection. In this paper, we have used ADDT, which facilitates a significant simpler computation of the test statistic instead of time domain cyclostationary detector which was used in our previous work [7], [21]. Moreover, the new field measurements also included collection of EDT statistics unlike previous measurements. The earlier work focused on the topics of cooperative sensing and distributed detection while these topics are not in the scope of this paper. On the other hand, this paper focuses only on spatial interpolation of sensing statistics including both energy and cyclostationary based test statistics.

This paper is organized as follows. Section II describes energy and cyclostationary based spectrum sensors along with their prototype platform that is used for collecting the measurement data. The details of the field measurement campaign are presented in Section III. Section IV focuses on the theory of spatial interpolation while Section V presents the results obtained from the measurement campaign. Finally, Section VI concludes the paper.

II. Energy and Cyclostationary Based Spectrum Sensors

A. System Model

The problem of detecting the existence of the primary user (PU) transmission can be modeled as a binary hypothesis test given by

$$\begin{aligned} H_0: &\quad x[n] = w[n] \\ H_1: &\quad x[n] = h[n] * s[n] + w[n], \end{aligned} \tag{1}$$

where n represents the discrete time index and " $*$ " denotes convolution operation while $x[n]$, $s[n]$, $h[n]$, and $w[n]$ denote the received signal, the PU signal, the channel impulse response and the additive white Gaussian noise (AWGN), respectively. In the conducted field measurements, the PU is OFDM based DVB-T signal which shows cyclostationary features, for example, due to the presence of cyclic prefix [22]. As the number of subcarriers in DVB-T is large (2K and 8K modes), the central limit theorem can be used to consider $s[n]$ to be Gaussian distributed. However, $s[n]$ are correlated random variables due to the presence of cyclic prefix [23]. Moreover, $w[n]$ and $s[n]$ are assumed to be independent of each other. It should be noted that the binary hypothesis test given by (1) is nominal and is used to conveniently explain different detectors presented in this paper. Field measurements generally involve several other factors affecting the desired signal such as shadowing, interference, and receiver non-idealities, etc.

Generally, the detector makes binary decisions based on the following rule

$$\begin{aligned} T < \eta &\rightarrow \text{Decide } H_0 \\ T \geq \eta &\rightarrow \text{Decide } H_1, \end{aligned} \tag{2}$$

where T is the scalar test statistic evaluated from the observations while the threshold η depends on the detection strategy and distribution of T under the two hypotheses. The two important performance parameters are probability of detection P_d and probability of false alarm P_f, and are given by

$$\begin{aligned} P_d &= \mathcal{P}(T \geq \eta | H_1), \\ P_f &= \mathcal{P}(T \geq \eta | H_0). \end{aligned} \tag{3}$$

In this paper, we consider Neyman-Pearson detector which maximizes the probability of detection with a constraint on the false alarm probability. Therefore, the threshold design depends only on the distribution of T under the null hypothesis H_0.

B. Energy Detection

The EDT statistic used in this paper is the RSSI (or the estimate of the input-signal power in dBm scale) denoted by $\hat{T}_E$ in dBm. The estimate of the input power at the absolute scale can be computed from N signal samples as

$$T_E = \frac{1}{N} \sum_{n=0}^{N-1} |x[n]|^2.$$

Note that NT_E follows chi-squared distribution as it is a sum of squares of Gaussian random variables. The calculated average power T_E is converted to $\hat{T}_E$ in dBm scale and compared with a threshold η_E to arrive at a decision D. The implementation of RSSI estimation following the A/D conversion is depicted in Fig.1.

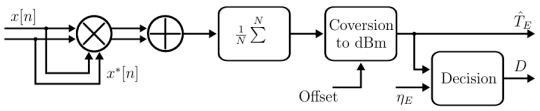

Fig. 1. Energy detector implementation.

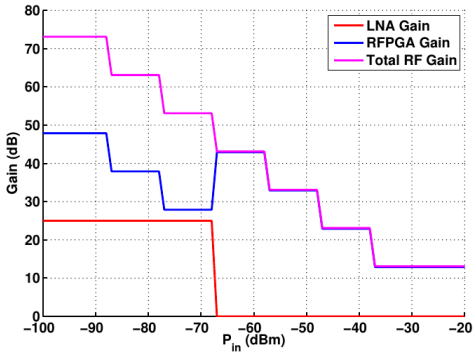

Fig. 2. Required front-end gain settings as a function of input power determined with laboratory measurements.

The conversion of the calculated average power T_E to $\hat{T}_E$ in dBm scale is done with a look-up table. This look-up table is calibrated by laboratory measurements to take into account the gain of the low noise amplifier (LNA) and variable gain amplifier of the analog front end. The required front-end gain is determined to be the maximum gain that does not saturate the A/D converter output. Measurements for the required gain settings for LNA and variable gain amplifier are depicted in Fig. 2. During the normal detection operation, the energy measurement starts with the maximum gain setting. If the linear range is exceeded, then the gain is reduced, correction factor is added to look-up table values and the measurement is repeated. The look-up table values and correct operation of RSSI are verified with laboratory measurements with frequencies 642 MHz (ch. 42) and 762 MHz (ch. 57). Verification measurements indicate reliable and accurate operation over input dynamic range from -120 dBm to -30 dBm, as depicted in Fig. 3. As the input power is decreased below -98 dBm, the input power estimate saturates, indicating the noise floor of the detector receiver chain.

C. Cyclostationary Detection

A cyclostationary process is a random process for which statistical properties vary cyclically with time. Most of wireless communication signals typically exhibit cyclostationarity at different cyclic frequencies related to the symbol rate, frequency, chip rate as well as their harmonics. As random noise is not cyclostationary, it is an attractive property for detecting PU signals and distinguishing them from noise [24]. Unlike energy detection, cyclostationary detector allows signal classification, performs reliably in low SNRs and is robust to noise uncertainty.

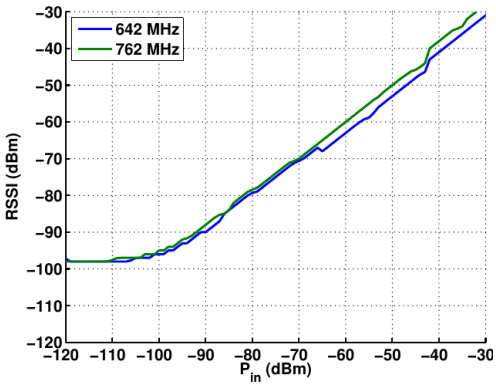

Fig. 3. Estimated received signal power as a function of input power.

An estimate of cyclic autocorrelation $\hat{R}(\alpha,\tau)$ can be evaluated [22] as

$$\hat{R}(\alpha,\tau)=\frac{1}{N}\sum_{n=0}^{N-1}x[n]x^*[n+\tau]e^{-j2\pi\alpha n}, \tag{4}$$

where $N+\tau$ is the number of received samples, α is the cyclic frequency of interest and τ is the time delay in samples. It is assumed that the signal is sufficiently oversampled to avoid aliasing in the cyclic frequency domain. The time delays are integer valued and $\alpha \in [0,1)$. In this paper, DVB-T is considered as the PU which uses OFDM transmission scheme. If N_d is the number of samples in the useful data of an OFDM symbol, N_c is the number of samples in cyclic prefix and $N_s = N_c + N_d$ is the number of samples in one OFDM symbol, then the OFDM signal exhibits cyclostationary features at cyclic frequencies k/N_s with $k \in \mathcal{Z}_+$ and peaks at $\tau = \pm N_d$. In this paper, we evaluate the presence of second-order cyclostationarity at $\alpha_1 = 1/N_s$ and $\tau_1 = N_d$.

There are several different implementations of cyclostationary detectors such as time domain cyclostationary detector, spatial sign correlation detector, and ADDT [8]. The implementation and performance comparison of these detectors have been carried out in [8]. In this paper, we have used ADDT instead of time domain cyclostationary detector, which was used in our previous work [7], as ADDT provides a significant simple computation of the test statistic. For ADDT, the test statistic is of the form

$$\Phi_n(\alpha,\tau)=\phi_x[n]-\phi_x[n-\tau]-\frac{2\pi\alpha n}{N} \tag{5}$$

for $n=0,1,\ldots,N-1$, where $\phi_x[n]=\angle x[n]$.

Under the null hypothesis H_0, the observations $x[n]$ are only Gaussian white noise so that $\Phi_n(\alpha,\tau)$ is uniformly distributed in $[-\pi,\pi]$ [25]. Under H_1, $\Phi_n(\alpha,\tau)$ is no longer uniformly distributed [25]. This is explained briefly as follows. In OFDM, N_c number of last samples out of N_d data samples in one OFDM symbols are copied in front of data samples to create a cyclic prefix. Therefore, when the samples are drawn from the part of the signal that belongs to the cyclic prefix for $\tau = N_d$, the first two terms in (5) cancel each other out as they have the same phase. The only term then left in (5) is the third term related to the cyclic frequency α. If $\alpha = 1/N_s$, then the samples corresponding to the cyclic prefix (i.e., $0,1,\ldots,N_c-1$) have exactly the same subset of angles $(2\pi\alpha n/N)$ that occur from one OFDM symbol to the next. This results in non-uniform distribution for sufficiently high SNR.

As the distributions of $\Phi_n(\alpha,\tau)$ under H_0 and H_1 are different (i.e., uniform and non-uniform, respectively), one can test for the presence of the PU signal by testing for the uniformity of $\Phi_n(\alpha,\tau)$ [25]. One way to do this in practice is to construct a histogram of B bins corresponding to angular domain sectors [25], [26]. By counting the samples falling into each bin, one can test how uniformly the samples are distributed. Under H_0 the angle is uniformly distributed and the number of samples in the bins are jointly multinomial distributed with sample size parameter N and probability vector $\mathbf{p} = [\frac{1}{B},\frac{1}{B},\ldots,\frac{1}{B}]$ [27]. If the number of samples in at least one of the sectors deviates from the expected value N/B more than a predetermined threshold η the null hypothesis is rejected and decision H_1 is made. Fig. 4 shows the implementation block diagram of the uniform distribution test of the cyclostationary detector with $B=4$ bins used for the field measurements of this paper. The test statistic used for this purpose, as shown in Fig. 4, is

$$T_C=\frac{2^{10}}{N}\max_{i=1\ldots4}|Y_i| \tag{6}$$

where Y_i for $i=1,2,3,4$ are the number of samples in the four angular bins minus $N/4$. Here $N/4$ is the expected value of the number of samples in each of the four bins under H_0. This way Y_i for $i=1,2,3,4$ can be modeled as zero mean random variables for convenience. The term $2^{10}/N$ in the test statistic comes from the fact that the test statistic T_C is represented in hardware using 10 bits. Multiplying by $2^{10}/N$ normalizes the value of $\max_{i=1\ldots4}|Y_i|$ between 0 and $2^{10}-1$ so that T_C is efficiently represented with 10 bits.

Next, we derive an approximation for the cumulative distribution function (CDF) of the local test statistics T_C under H_0 as computed in Fig. 4. The distribution under H_0 is needed for designing the decision threshold η for the Neyman-Pearson detector while the distribution of the test statistic under H_1 is not necessary. The joint distribution of the number of samples in the four angular bins in Fig. 4 is the multinomial distribution with sample size parameter N and probability vector $\mathbf{p} = [\frac{1}{4},\frac{1}{4},\frac{1}{4},\frac{1}{4}]$. It is known that the multinomial distribution can be approximated by a multivariate normal distribution when the sample size N is large and when the elements of $\mathbf{p}$ are not close to 0 or 1 [27], [28]. In our case

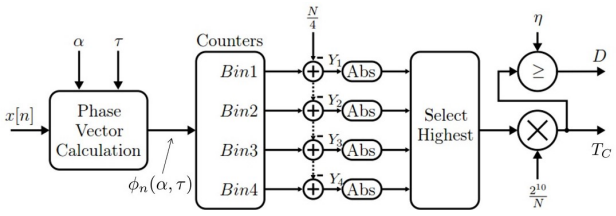

Fig. 4. The block diagram of the uniform distribution test implemented in [26].

the sample size N is between 2^{15} and 2^{17} and the elements of $\mathbf{p}$ are all $\frac{1}{4}$, and hence we can expect the multivariate normal distribution to provide a good approximation. That is, the joint distribution of the number of samples in the 4 bins can be approximated as $\mathcal{N}(N\mathbf{p}, \Sigma)$, where [27]

$$\mathbf{\Sigma}_{ij} = \begin{cases} \frac{3N}{16}, & \text{if } j = i \\ \frac{-N}{16}, & \text{if } j \neq i. \end{cases}$$

Subtracting the expected value $N/4$ from the sample sizes of each angular bin (as done in Fig. 4) we obtain that the joint distribution of $\{Y_1, Y_2, Y_3, Y_4\}$ can be approximated by $\mathcal{N}(\mathbf{0}, \Sigma)$, where $\mathbf{0} = [0, 0, 0, 0]$. Denote the multivariate normal CDF with mean $\mathbf{0}$ and covariance matrix Σ as $F(z_1, z_2, z_3, z_4)$. The CDF of the test statistic T_C can be then approximated as

$$\begin{aligned} \mathrm{P}(T_C \leq \tilde{z}) &= \mathrm{P}(\max_{i=1\ldots4} |Y_i| \leq z) \\ &= \mathrm{P}(-z \leq Y_1 \leq z, \ldots, -z \leq Y_4 \leq z) \\ &\approx F(z, z, z, z) - \sum_{(u_1,\ldots,u_4)\in\tilde{\mathcal{U}}} F(u_1 z, u_2 z, u_3 z, u_4 z), \end{aligned} \tag{7}$$

where $\tilde{z} = \frac{2^{10}}{N} z$, $F(.)$ is the joint CDF of $\{Y_1, Y_2, Y_3, Y_4\}$, $\tilde{\mathcal{U}} = \mathcal{U} \setminus (1, 1, 1, 1)$ and $\mathcal{U} = \{\mathbf{u} : \mathbf{u} = (u_1, u_2, u_3, u_4),$ with $u_i = \pm 1, \forall 1 \leq i \leq 4\}$. In (7) the first term corresponds to the probability that all $Y_1, \ldots, Y_4$ are less than z, whereas the subtracted sum term corresponds to the probability that at least one of $Y_1, \ldots, Y_4$ is less than $-z$.

Fig. 5 shows the CDF of T_C under H_0 evaluated by three methods: empirical CDF, analytically approximated CDF and CDF based on the measurements in a anechoic chamber (or Faraday's cage). The empirical CDF is estimated from 100000 simulations while the analytically approximated CDF is given by (7) that uses the normal approximation. The empirical distribution under H_0 has been estimated from simulated test statistics generated according to Fig. 4 by feeding the counters uniformly distributed random angles between $-\pi$ and π. The number of test statistics per channel measured in Faraday's cage is 2000. The number of samples in this example is $N = 2^{17}$. It can be seen that the theoretical approximation is practically on top of the empirical CDF while the CDF based on the Faraday's cage measurement is also very near to these two curves.

D. Spectrum Sensor Prototype

A spectrum sensor prototype, depicted in Fig. 6(a) was used for collecting the field measurement data reported and analyzed in this paper. The sensor platform is specifically designed for mobile usage and it can be embedded to a mobile phone. In this paper, we have used the sensor separately by interfacing it to a PC through a USB port.

Fig. 6(b) shows the functional description of the sensor platform. It consists of two RF front-ends (for DVB-T and WLAN), A/D-converters (ADCs) for both front-ends, a field programmable gate array (FPGA) that features two soft microcontrollers, and a USB communication bridge for interfacing purposes. The FPGA is used for the implementation of the

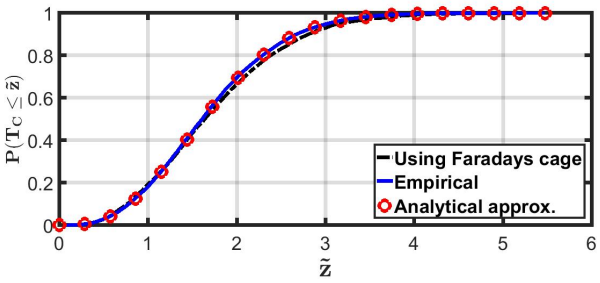

Fig. 5. Figure shows three CDFs for ADDT: empirical CDF, the CDF computed using the normal approximation in (7), and the CDFs computed from measurements in a Faraday's cage. The number of samples in this example is $N = 2^{17}$ and the number of simulations used to compute the empirical CDF is 100000.

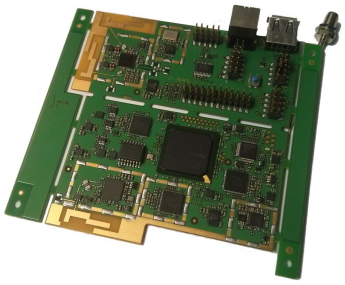

(a) Prototype platform

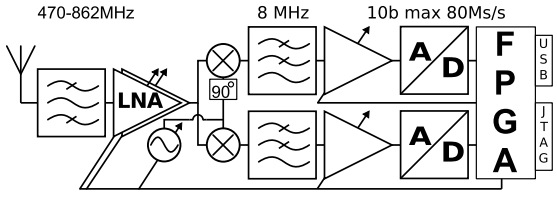

(b) Sensor Functionalities

Fig. 6. Spectrum sensor prototype platform and description of spectrum sensor functionalities.

actual signal detection algorithms, digital baseband and controlling schemes. Further details on the implementation of the platform are presented in [26], [29].

Fig. 7 depicts the probability of detection as a function of input power with different detection times for the ADDT. The number of measurements used to estimate the probability of detection is 2000 while the constraint on the false alarm probability is 5%. In the corresponding laboratory measurement, the test signal is fed directly to the RF input of the detector from a vector signal generator. For practical reasons, detection time of 14.4 ms was used in the field measurement since it allowed the acquisition of several hundreds of detections in reasonable time and is still adequate for demonstrating the spatial estimation of test statistics.

It is important to note here that the use of FPGA in this paper is for experimental purpose. Also, this particular test board embodiment does not exactly fit in a mobile phone. However, its predecessor in [29] has been fit in Nokia N900 phone and the detector used in this paper is a simplified version of the predecessor. Moreover, the detector implementation

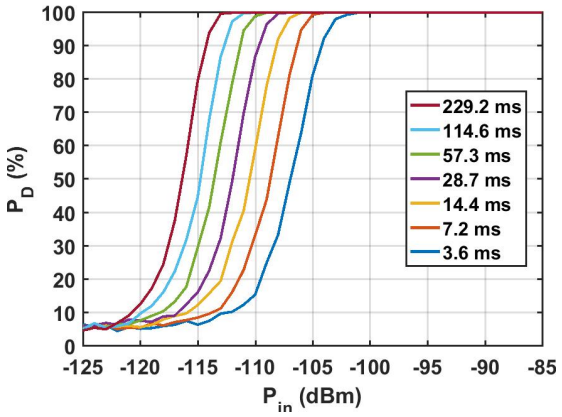

Fig. 7. Detection probability of ADDT for different sensing times as a function of input power fed to the antenna port of the detector implementation.

employed in this paper is a viable technique for cognitive radios considering the current state-of-the art of the sensor hardware. Although there could be further optimization in detector architecture like in [30], where a state of the art cognitive spectrum sensor with extremely low power is presented, the intended focus of this paper is application of mobile detection and not on the hardware optimization.

III. Field Measurements

The field measurement campaign was carried out in sub-urban Espoo region, where four sensors were used in 31 different cluster-locations. At each cluster-location, the four sensors were spread at least 100 meters apart from each other. Thus, there are a total 124 measurements locations for the measurement campaign as depicted by Fig. 8. At each measurement location, 400 test statistics samples were collected with both the detectors (ADDT and EDT) on DVB-T channels 42-49. While collecting these samples, the following additional data was also collected for each sample: time-stamp (in sec), location coordinates (latitude and longitude in WGS84 format), and frequency of operation (in MHz). The measurement data was collected using a laptop and later processed offline using ArcGIS. Detection time of 14.4 ms was used. Although this does not satisfy the FCC sensitivity requirements for individual detections, the standards can be met through data fusion of multiple detections from a single or multiple sensors [7], [21].

Fig. 9 depicts three DVB-T transmitter locations relative to the measurement campaign for representative channels of 45, 46 and 47 while the corresponding transmitter parameters are presented in Table I. The three channels 45, 46 and 47 represent *partially-occupied*, *occupied* and *free* channels, respectively, in the measurement region. This classification is based on the ability of decoding the TV signal in the region which was verified by doing measurements in the Helsinki city-center using Rohde & Schwarz TSM-DVB T/H diversity test receiver [31] earlier. Note that decoding the signal requires several dB higher signal strength as compared to only detecting the signal.

TABLE I
DVB-T transmitter parameters for representative channels 45 (partially occupied), 46 (occupied) and 47 (free) [7]

DVB-T Trans.	Espoo	Tallinn	Nummi-Pusula
Latitude	60.1778	59.4713	60.45
Longitude	24.6403	24.8875	23.8833
Mast Height	313 m	289 m	70 m
Trans. Power	47 dB	42 dB	12 dB
Trans. Channels	44, 46	45	42, 47

Two DVB-T transmitters clearly contribute to the measurement results. One is located in Espoo and is transmitting on channels 44 and 46 with high power. Since the measurements are carried out in Espoo area, the aforementioned channels were always detected in all the measurement locations. The other transmitter, transmitting on channel 45, is located in Tallinn, Estonia, which is approximately 80 kilometers south of the measurement region and across the Baltic sea. The transmission from this transmitter can be decoded mainly near the shore and on high ground while the signal can be detected in most parts of the measurement region. The received signal powers for channels other than 44, 45, and 46 are pretty weak in the measurement region as shown in our earlier work [7]. Channel 47 is taken as representative of a free channel and its nearest transmitter is located approximately 55 km north-east of the measurement region in Nummi-Pusula.

IV. Spatial Interpolation Techniques

In this paper, we have considered IDW as a representative of deterministic interpolation techniques while for statistical methods, we have considered Kriging, specifically ordinary Kriging (OK) and universal Kriging (UK). These spatial interpolation methods are described in this section. This is followed by the details on performance criteria and the use of ArcGIS software for spatial interpolation.

A. Inverse Distance Weighing (IDW)

IDW is the deterministic interpolation that follows the basic law of geology: things that are closer will have more impact than the ones which are farther away [15]. It is also known as *Shepard's method*. Let us denote a location $\mathbf{s} = [x\ y]^T$ with x and y being the longitude and latitude values of the location. If we denote $Z(\mathbf{s}_i)$ as the parameter values at the measured locations $\mathbf{s}_i$ for $i = 1, \ldots, M$, then the parameter value at an unmeasured location $\mathbf{s}$ may be estimated using IDW in terms of the parameter values at the M measured locations by

$$\hat{Z}(\mathbf{s}) = \begin{cases} \frac{\sum_{i=1}^{M} w_i(\mathbf{s}) Z(\mathbf{s}_i)}{\sum_{i=1}^{M} w_i(\mathbf{s})}, & d(\mathbf{s}, \mathbf{s}_i) \neq 0 \ \forall i \\ Z(\mathbf{s}_i) & \text{Otherwise,} \end{cases} \tag{8}$$

where the weight factor $w_i(\mathbf{s})$ depends on the distance $d(\mathbf{s}, \mathbf{s}_i)$ between the measured locations $\mathbf{s}_i$ and predicted location $\mathbf{s}$ and is given by

$$w_i(\mathbf{s}) = \frac{1}{d(\mathbf{s}, \mathbf{s}_i)^p}, \tag{9}$$

where p is the power exponent and i is the index of the measured locations. Here weight decreases as distance increases from the interpolated points. The value of p controls the rate at

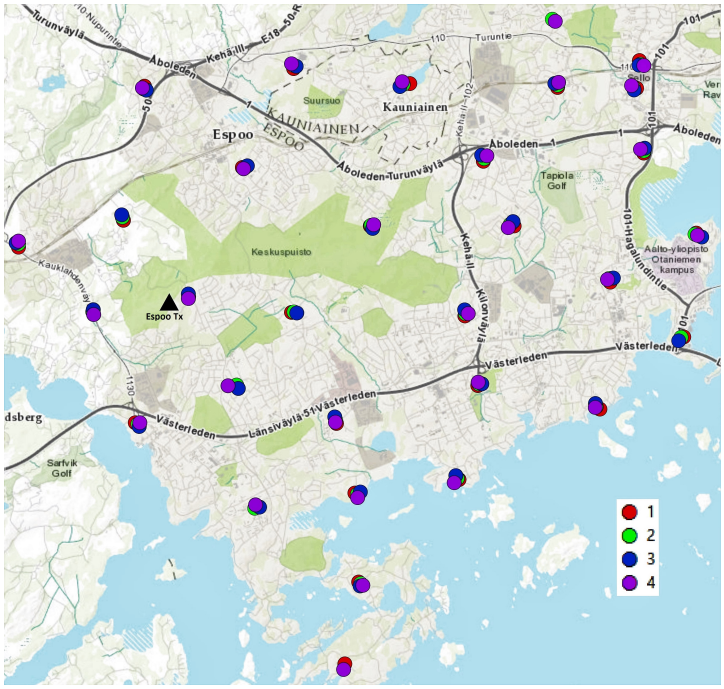

Fig. 8. Field measurement data prior to spatial estimation. The color of the dots corresponds to the sensor index. Although the four sensors look very close at each measurement location; they were at least 100 m apart from each other.

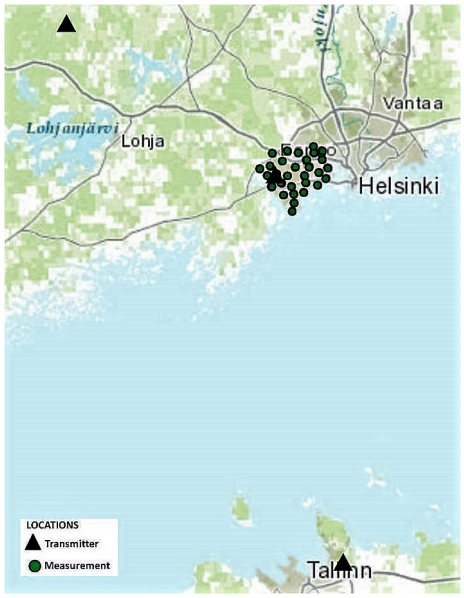

Fig. 9. Transmitter locations for representative channels of 45, 46, and 47 with respect to measurement locations.

which the weight of a measurement point drops as a function of the distance to the interpolated point. The value of $p = 2$ is widely used for which the method is known as the *inverse distance squared weighted interpolation*. However, there is no theoretical justification to prefer this value over others and the optimal value of p for a given scenario or application should be evaluated through cross-validation.

B. Kriging

Kriging is a statistical interpolation technique where the knowledge about the spatial statistics of the measured field is used for interpolation. It is essentially a two-stage procedure that generates an estimated surface from scattered data points with z-values, which are the field measurement metrics in this paper. The first stage is to calculate the weight factor at a given location using spatial auto-correlation of sampled data (which is known as semivariogram) while the second stage involves estimation of values at that location using weighted sampled data. In Kriging, the weighting is based on a statistical calculation of the spatial correlation between the data points. Extensive theory of variography and Kriging can be found in [16], [32].

1) Semivariogram: The Kriging procedure begins with modeling of the functions that estimate the spatial dependence of the measured values, or in other words, their *spatial auto-correlation* [14]. Spatial modeling, also known as *variography*, usually involves a graph of empirical semivariogram (see Fig. 10), which illustrates the semivariances for all pairs of data of a measurement location. For a pair of locations $\{\mathbf{s}_i, \mathbf{s}_j\}$ the semivariogram can be calculated as

$$\hat{\gamma}(\mathbf{s}_i, \mathbf{s}_j) = \frac{1}{2}(Z(\mathbf{s}_i) - Z(\mathbf{s}_j))^2, \tag{10}$$

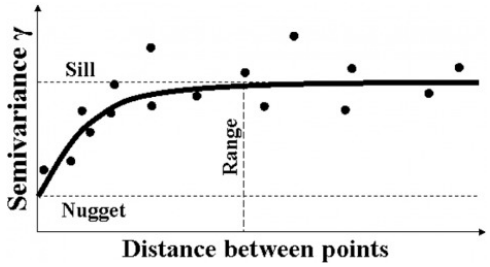

Fig. 10. Example of semivariance and a variogram model from [33].

where $\hat{\gamma}(\mathbf{s}_i, \mathbf{s}_j)$ is the semivariance for a location pair $\{\mathbf{s}_i, \mathbf{s}_j\}$. Since measurements are rarely made using regular uniform grid of measurement points, there are often several location pairs such that the resulting variogram would become difficult to analyze and be sensitive to outliers. Hence, a *binned variogram*, that divides the location pairs to a limited number of distance classes, is often used [16]. It can be considered as a moving average of the semivariance cloud.

2) Fitting a Variogram Model: After obtaining the semivariance plot, a *variogram* model needs to be fitted to the data. Fig. 10 depicts a generic example of empirical semivariances and an exponential fitted model [33]. Commonly used models for the variograms are *circular, spherical, exponential, Gaussian,* and *stable*. Expressions for these models are given in Table II. Once the variogram model is chosen, the optimal parameters for the model can be found using mathematical methods such as least squares (LS), weighted LS or residual maximum likelihood.

Fig. 10 also introduces the terms *sill, nugget,* and *range*.

TABLE II
SEMIVARIOGRAM MODELS WITH THEIR EQUATIONS. HERE h IS THE DISTANCE BETWEEN TWO POINTS, θ_r IS THE RANGE, θ_s IS THE SILL, AND $\boldsymbol{\theta} = [\theta_s\ \theta_r]^T$.

Model	Equation
Circular	$\gamma(h;\boldsymbol{\theta}) = \begin{cases} \frac{2\theta_s}{\pi}\left[\frac{\|h\|}{\theta_r}\sqrt{1-\left(\frac{\|h\|}{\theta_r}\right)^2} + \arcsin\frac{\|h\|}{\theta_r}\right] & \text{for } 0 \le \|h\| \le \theta_r \\ \theta_s & \text{for } \theta_r \le \|h\| \end{cases}$
Spherical	$\gamma(h;\boldsymbol{\theta}) = \begin{cases} \theta_s\left[\frac{3}{2}\frac{\|h\|}{\theta_r} - \frac{1}{2}\left(\frac{\|h\|}{\theta_r}\right)^3\right] & \text{for } 0 \le \|h\| \le \theta_r \\ \theta_s & \text{for } \theta_r \le \|h\| \end{cases}$
Exponential	$\gamma(h;\boldsymbol{\theta}) = \theta_s\left[1-\exp\left(-3\left(\frac{\|h\|}{\theta_r}\right)\right)\right]$ for $\forall h$
Gaussian	$\gamma(h;\boldsymbol{\theta}) = \theta_s\left[1-\exp\left(-3\left(\frac{\|h\|}{\theta_r}\right)^2\right)\right]$ for $\forall h$
Stable	$\gamma(h;\boldsymbol{\theta}) = \theta_s\left[1-\exp\left(-3\left(\frac{\|h\|}{\theta_r}\right)^{\theta_e}\right)\right]$ for $\forall h$

Range θ_r is the distance at which the semivariance γ reaches 95% of the final value it converges to, or in practice, where the model first flattens. *Sill* θ_s is the semivariance value at which the theoretical variogram model attains the range. *Nugget* ν is a non-zero value at infinitely small separation distance, which is basically consequence of measurement errors of the data as well as the variation occurring at distances below the smallest sampling interval. In addition to the terms presented in the figure, *partial sill* θ_p is defined as the value of sill relative to nugget, i.e., $\theta_p = \theta_s - \nu$. The covariance of the random field $C(\mathbf{s}_i, \mathbf{s}_j)$ can be determined using the spatial auto-correlation of the sampled data, and it is given by

$$C(\mathbf{s}_i, \mathbf{s}_j) = \theta_s - \gamma(h), \tag{11}$$

where h denotes the distance between points $\{\mathbf{s}_i, \mathbf{s}_j\}$.

3) Estimation at unmeasured locations: After the modeling of spatial autocorrelation is completed, the estimation phase can be carried out. The general formula for the estimated value $\hat{Z}(\mathbf{s})$ using the Kriging estimator is given by

$$\hat{Z}(\mathbf{s}) = \sum_{i=1}^{M} \lambda_i(\mathbf{s})[Z(\mathbf{s}_i) - \upsilon(\mathbf{s}_i)] \ + \upsilon(\mathbf{s}), \tag{12}$$

where $\lambda_i(\mathbf{s})$ is the weight factor and $\upsilon(\mathbf{s})$ is the trend component at the location $\mathbf{s}$. Now, the estimation error can be expressed as

$$\hat{Z}(\mathbf{s}) - Z(\mathbf{s}) = \left[\hat{Z}(\mathbf{s}) - \upsilon(\mathbf{s})\right] - [Z(\mathbf{s}) - \upsilon(\mathbf{s})] = \hat{R}(\mathbf{s}) - R(\mathbf{s}), \tag{13}$$

where $\hat{R}(\mathbf{s}) \triangleq \hat{Z}(\mathbf{s}) - \upsilon(\mathbf{s})$ and $R(\mathbf{s}) \triangleq Z(\mathbf{s}) - \upsilon(\mathbf{s})$ are residual components of the estimated and true values at the unmeasured location, respectively. Basically, the trend component $\upsilon(\mathbf{s})$ of the given random field $Z(\mathbf{s})$ can be represented as a deterministic function. Therefore, instead of interpolating $Z(\mathbf{s})$ the trend component $\upsilon(\mathbf{s}_i)$ is removed from the sampled data values $Z(\mathbf{s}_i)$ and Kriging interpolation estimates the residuals $R(\mathbf{s})$ using (12) as

$$\hat{R}(\mathbf{s}) = \sum_{i=1}^{M} \lambda_i(\mathbf{s}) R(\mathbf{s}_i). \tag{14}$$

After interpolating the residual components, it is added back with the trend component to get the estimated value at unknown location $\hat{Z}(\mathbf{s})$ as given by (12).

Now for estimating the interpolated residuals $\hat{R}(\mathbf{s})$ using (14), the weight vector $\boldsymbol{\lambda}(\mathbf{s}) = [\lambda_1(\mathbf{s}) \ldots \lambda_M(\mathbf{s})]^T$ is chosen such that the mean square error (MSE) in estimating residuals $R(\mathbf{s})$ is minimized. Such weight vector is given [16], [32] by

$$\boldsymbol{\lambda}(\mathbf{s}) = \mathbf{C}^{-1}\mathbf{c}(\mathbf{s}), \tag{15}$$

where $\mathbf{C}$ is the covariance matrix between sampled data points with elements $\mathbf{C}_{i,j} = C(\mathbf{s}_i, \mathbf{s}_j)$ and $\mathbf{c}(\mathbf{s})$ is vector with covariances between sampled data points and estimation points i.e., $\mathbf{c}_i = C(\mathbf{s}_i, \mathbf{s})$. The covariance values in matrix $\mathbf{C}$ can be calculated using semivariogram values and its parameters, as given in (11). The weight factor λ decreases with increasing distance, i.e., the sample points within local neighborhood will have more influence than the points which are placed far away.

Based on the assumption of trend component, Kriging can be classified as *simple Kriging, ordinary Kriging (OK)* and *universal Kriging (UK)*. In simple Kriging, the trend component $\upsilon(\mathbf{s})$ is assumed to be known and constant whereas in ordinary Kriging it is assumed to be constant but unknown. OK is the default Kriging method as it doesn't need the knowledge of the trend, and it is more practically applicable compared to other Kriging methods. In UK, the trend component will be the first or higher order polynomial of (x, y) location coordinates. The Kriging estimator $\hat{Z}(\mathbf{s})$ as in (12) is the linear combination of M weight factors ($\boldsymbol{\lambda}(\mathbf{s})$) scaled residual components. The weights can be obtained by solving a system of linear equations with the complexity of O(n^3). To reduce the complexity

TABLE III
DIFFERENT KERNEL FUNCTIONS CONSIDERED IN THIS PAPER. FOR ALL FORMULAS BELOW, $\alpha = \frac{r}{\beta}$ WHERE r IS A RADIUS (CENTERED AT POINT s), β IS THE BANDWIDTH PARAMETER, AND $\mathcal{I}_{(\cdot)}$ IS AN INDICATOR FUNCTION.

Model	Equation
Constant	$\mathcal{I}_{(s-h<s_i<s+h)}$
Exponential	$e^{-3\alpha}$
Gaussian	$e^{-3\alpha^2}$
Epanechnikov	$1-\alpha^2$ for $\alpha < 1$
Quartic	$\left(1-\alpha^2\right)^2$ for $\alpha < 1$
Polynomial5	$1-\alpha^3\left(10-\alpha\left(15-6\alpha\right)\right)$ for $\alpha < 1$

to O(n), kernel approximations to the weight function has been proposed in [34] and so $\hat{Z}(\mathbf{s})$ can be calculated at each point $\mathbf{s}$ without any initial matrix computations. Table III shows different kernel functions considered in this paper such as *constant, exponential, Gaussian, Epanechnikov, quartic*, and *polynomial5* [35]. All these kernel interpolations use the radial symmetry which significantly reduce the computational complexity. Appropriate function can be selected based on its goodness of fit. However, the accuracy for UK degrades if the assumed models are different from the actual models [34]. Various other Kriging methods are thoroughly described and analyzed in [36] and [37]. In this paper, we have adopted OK and UK which have been observed to work efficiently in the considered scenario.

C. Cross Validation

Cross validation is a process of determining the accuracy of the estimates of the interested parameter values at the unmeasured locations. In this process, one sampled data is removed and remaining samples are used to estimate the value at the removed sample location. This process is repeated for each sample data, and cross validation metrics are calculated. There are several metrics such as mean error, root mean square error (RMSE), average Kriging standard error, and RMS standardized error. In this paper, we have considered the widely used RMSE as a metric for the accuracy of prediction for both deterministic and statistical interpolation techniques. For good estimation accuracy, the value of RMSE should be sufficiently low.

D. Use of ArcGIS

Geographic information system (GIS) deals with capturing, storing, analyzing, and interpreting the spatial data to understand patterns, trends and relationships. It plays predominant role in continuous data analysis. It defines certain methodologies for creating a continuous surface from the sampled data. ArcGIS is a software for GIS, developed and owned by Environmental Systems Research Institute (ESRI) group of Redlands, California. It is simple to use and provides user friendly environment to analyze and perform operations on spatial data. It also provides solid documentation to understand the broad functionalities involved in the spatial data analysis. ArcMap is a component of ArcGIS where we can visualize the spatial data and can perform more analysis on it. It can create maps by compiling spatial data and analyze the information on the map to provide realistic solutions in various applications. In this paper, *Geo-statistical analysis* extension in ArcMap is utilized for various deterministic and geostatistical spatial interpolation methods. It conducts analysis on the data based on certain attributes from various locations in landscape and interpolates it to construct continuous surface. Quality of the generated surface can be assessed through cross validation. In this work, we have used ArcGIS 10.3 for our spatial analysis on field measurements to construct REM using spatial interpolation techniques. For more details on ArcGIS software, please refer to [38].

V. Results and Analysis

This section starts by presenting the measured test statistics for energy and cyclostationary detectors, i.e., EDT and ADDT statistics for the representative channels. This is followed by an example of interpolating ADDT statistics using OK with exponential fit. Next, the effects of different fitting functions for OK are studied. Comparison is then carried out for different spatial interpolation techniques including IDW, OK and UK for ADDT statistics. Later, spatial interpolation results are presented for EDT and ADDT statistics showing the benefits of using cyclostationary detector. Note that for all spatial interpolation schemes, average of the 400 collected measured test statistics per channel per location is taken as the measured value $Z(\mathbf{s}_i)$ at each measured location. The sensing time corresponding to each test statistic is 14.4 ms.

A. Statistics of ADDT and EDT

Figs. 11 and 12 show the ADDT and EDT values, respectively, as a function of distance from the corresponding DVB-transmitter for the three representative channels: (a) 45 (partially occupied), (b) 46 (occupied), and (c) 47 (free). For channel 46, both ADDT and EDT values are very high as the measurement region is inside the expected coverage region for this channel. On the other hand, for channel 47, both the measured statistics are very low valued. For channel 45, the effect of fading and shadowing can be seen on the test statistics, where both the measured statistics are moderate. Because of fading and shadowing effects, there are lot of fluctuations in the measured values at the same location. However, on average, there is significant decay in these test statistic values as the distance from the transmitter increases.

B. Example of interpolating ADDT statistics using OK

Figs. 13 and 14 show the results of spatial interpolation for channels 45, 46 and 47 using exponential fit for OK and considering all neighbors. Fig. 13 shows the exponential fit for the considered data while Fig. 14 shows the corresponding spatial interpolation map of ADDT statistics in the measurement region. Here one map is computed assuming $Z(\mathbf{s}_i)$ to be the average of the 400 samples measured at location $\mathbf{s}_i$. Note that the symbology or color mapping for the spatial interpolation in the above figures is not linear and has been optimized for visual representation while making sure that the same scales can be used for all the channels.

Fig. 14 shows that the values of interpolated ADDT statistics for channel 45 are moderate towards southern part of measurement region while low towards northern parts. For channel 46, as expected, the interpolated test statistics are high valued throughout the measurement region. The interpolated test statistics for channel 47 are mostly low valued except for slightly higher values for the locations near Espoo transmitter. This is due to the interference caused by the strong signal in the adjacent channel 46.

From Fig. 14, it can be observed that the results show estimates of the test statistic over the sea which may be outside the convex hull (or polygon of minimum area) that contains

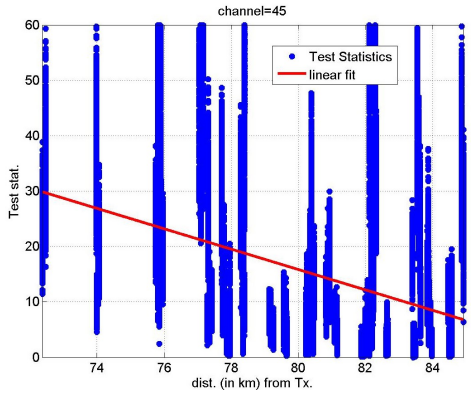

(a) Channel 45

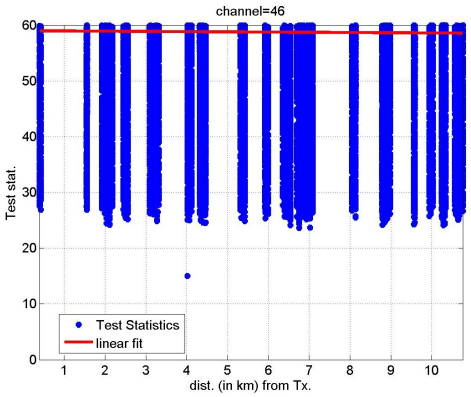

(b) Channel 46

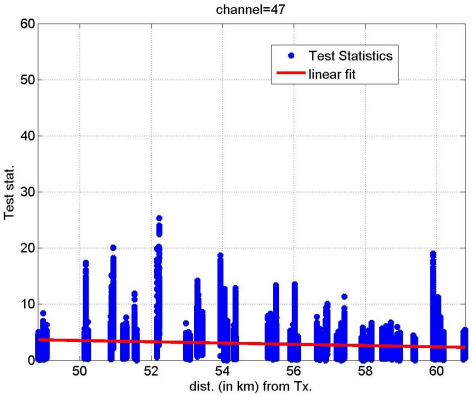

(c) Channel 47

Fig. 11. ADDT statistics vs. distance for the three representative channels: (a) 45 (partially occupied), (b) 46 (occupied), and (c) 47 (free).

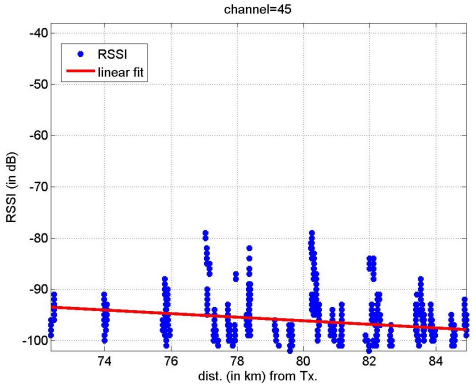

(a) Channel 45

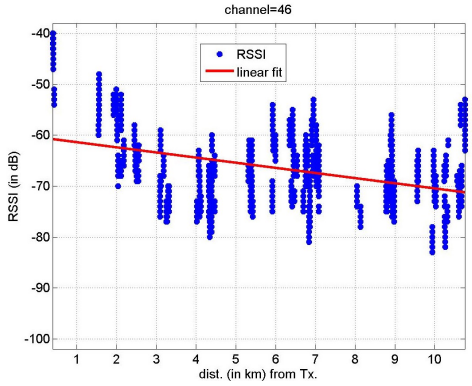

(b) Channel 46

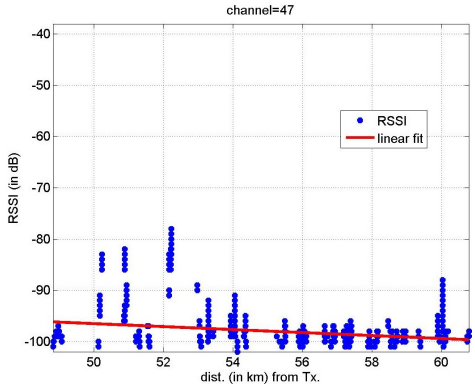

(c) Channel 47

Fig. 12. EDT statistics (RSSI in dBm) vs. distance for the three representative channels: (a) 45 (partially occupied), (b) 46 (occupied), and (c) 47 (free).

all the measurement locations. This is because geostatistical analyst tool of ArcGIS interpolates the values of the test statistic at all locations that lie within the minimum spatial bounding box (i.e., smallest rectangle encompassing all the input measurement locations). Thus, ArcGIS is doing extrapolation in the region of minimum spatial bounding box outside the convex hull. However, such region is minimal in area and still close to measurement points. Note that the accuracy of extrapolation starts degrading as one gets farther away from the measurement points [38]. Moreover, the RMSE calculation is carried out only over measured points so that the errors in extrapolation do not affect the RMSE calculation.

TABLE IV
ORDINARY KRIGING USING EXPONENTIAL FIT FOR CHANNELS 45, 46 AND 47.

Channel	Nugget	Partial Sill	Range	RMSE
45	79.308	144.87	0.0602	10.466
46	12.076	4.6785	0.0096	3.6938
47	2.3875	1.7831	0.0461	1.836

Table IV shows the values of nugget, partial sill and range along with RMSE. Channel 45 has the highest nugget value

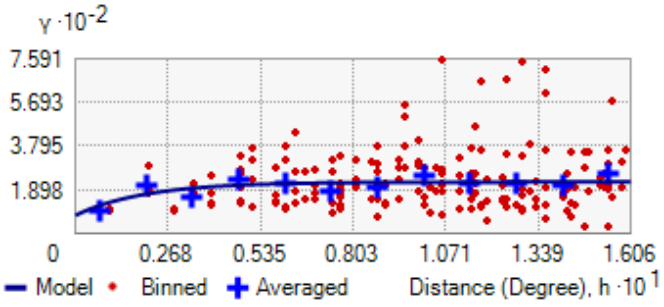

(a) Channel 45

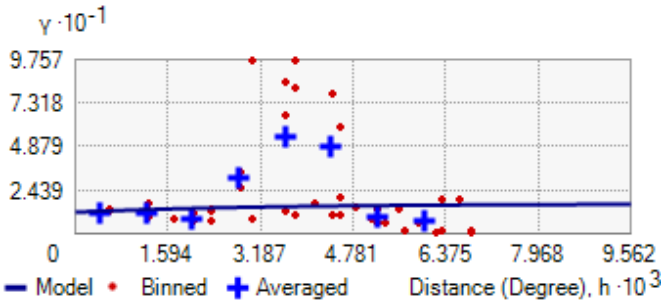

(b) Channel 46

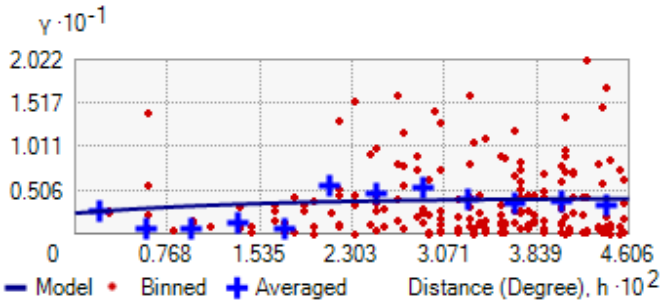

(c) Channel 47

Fig. 13. Exponential fit for ADDT statistics based variogram for channels 45, 46, and 47.

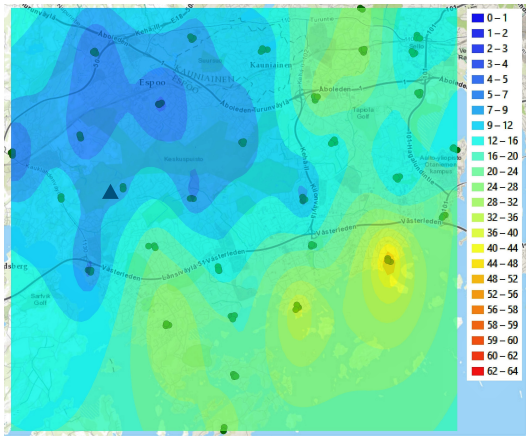

(a) Channel 45

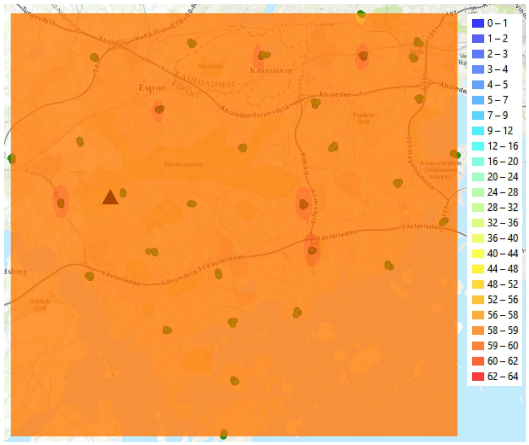

(b) Channel 46

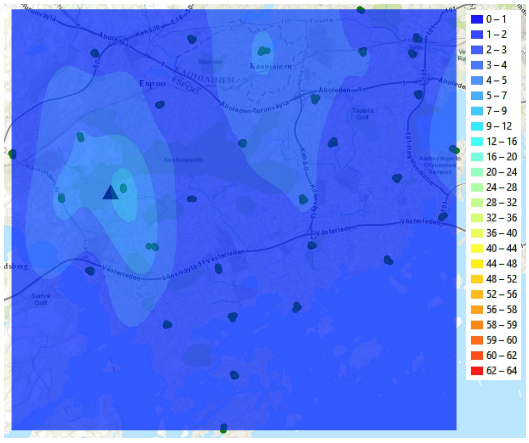

(c) Channel 47

Fig. 14. Spatial interpolation maps of ADDT statistics for channels 45, 46, and 47 using exponential fit and OK.

indicating that the points closer are highly dissimilar. Even the range is highest for Channel 45. Note that the length of a degree of latitude and longitude corresponds to 111.132 km and 78.847 km respectively. Assuming the average length of a degree to be 95 km, the range for OK for channels 45, 46 and 47 are 5.718 km, 0.912 km, and 4.379 km respectively. Fig. 15 shows the number of neighbors at each measurement location for two different values of range of 2.5 km and 5.5 km. For the range values of 2.5 km and 5.5 km, the average number of neighbors at a measurement location are 13.3 and 49.3 respectively. It can be also observed from Table IV that the RMSE is highest for channel 45 followed by channel 46 and channel 47. The reason is that variation is large across channel 45 while it is low for channels 46 and 47. Although variation is low for channel 46, as the test statistic values are high, the RMSE is higher as compared to the case of channel

47 which has low values of test statistics.

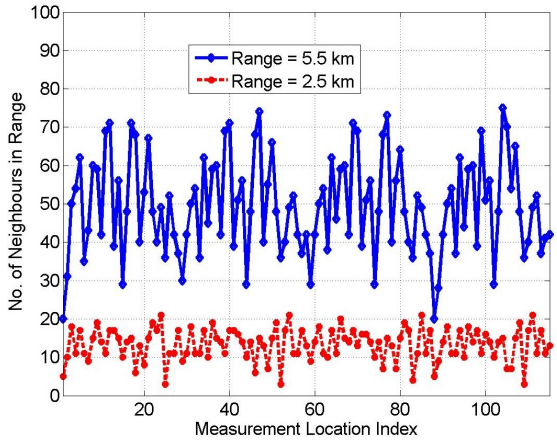

Fig. 15. The average number of neighbors at a measurement location in the range are 49.3 and 13.3 for the range values of 5.5 km and 2.5 km respectively.

C. Comparison of different fitting functions

Table V shows results for OK with different fitting functions for channel 45. Although the RMSE values for all the fitting functions are in the same order, exponential fit has the lowest RMSE among the tested fitting functions for the considered scenario.

TABLE V
OK WITH DIFFERENT FITTING FUNCTIONS FOR CHANNEL 45.

Model	Nugget	Partial Sill	Range	RMSE
Circular	73.1195	141.3847	0.0233	10.5499
Exponential	79.308	144.87	0.0602	10.466
Spherical	71.8615	142.3076	0.0249	10.5693
Gaussian	80.8232	133.6944	0.027	10.4934
Stable	28.243	174.3704	0.1112	10.5337

D. Comparison of different spatial interpolation techniques

Fig. 16 and Table VI compare the performances of IDW, OK, and UK for channels 45, 46 and 47 respectively. For IDW optimal p is used while for OK and UK, optimal fitting models are used. Furthermore, optimal kernel models are used for UK.

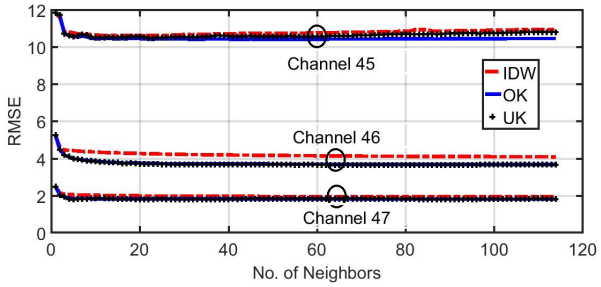

Fig. 16. Effect of number of nearest measurement points used for interpolation for ADDT.

Fig. 16 shows the effects of number of participating neighbors in spatial interpolation. It can be seen that there is big drop in RMSE for all the schemes for as few as 5-10 neighbors. After that the error reduces slowly but monotonically for OK. On the other hand, the error increases for IDW and UK after certain number of neighbors. For OK, the error decreases as any neighbor added to the spatial interpolation technique would either reduce the error or would be assigned negligible weight. For UK, the error increases as there is difference between assumed and actual kernel functions for the trend. For example, the actual trend for this scenario is of the eighth order while ArcGIS only allows at most third order polynomial. For IDW, the weights are based on distance and not on spatial correlation between the points. Therefore, even distant but uncorrelated neighbors may have non-zero weights and thus adding to the error.

Table VI compares different spatial interpolation methods: IDW, OK and UK. Note that IDW is deterministic model and does not need quantities such as fitting model, kernel function, and polynomial order. As such, they are mentioned as not applicable (NA) for IDW. Similarly, the kernel function and polynomial order is only needed for UK where it is assumed that the trend is known. For all the schemes, optimal nearest neighbors are used. It can be seen that UK gives the best performance among the considered schemes for channels 46 and 47 while OK gives a better performance for channel 45. Note that the performance of UK depends on the choice of fitting function for the trend component. For example, ArcGIS only gives option till third order while the trend for channel 45 is of the eighth order polynomial. The mismatch between the assumed and actual trend increases the error slightly. It should be noted that OK performs pretty well in such situations with much lower complexity.

E. Comparison of EDT and ADDT

Fig. 17 shows the results of spatial interpolation of EDT values for channels 45, 46, and 47 using OK with exponential fitting. The test statistic values for channel 46 are mostly high as expected. Although test statistic values for channel 47 are mostly low, there is increase in values near the Espoo transmitter. This is the result of interference from adjacent channel 46, which is being transmitted from the Espoo transmitter. For channel 45, the test statistics take high values in the southern part of the measurement region and near the Espoo transmitter. Note that there is also adjacent-channel-interference in channel 45 from channels 44 and 46.

Figs. 18 and 19 show the estimated occupied and unoccupied regions for channels 45 and 47, respectively, using the two detectors. For both the detectors, threshold is designed assuming Neyman-Pearson detectors with a constraint on the false alarm of 5%. The threshold values have been calculated empirically for each detector by measuring 2000 test statistic values per channel in an anechoic chamber (or Faraday's cage) to simulate the null hypothesis scenario. Accordingly, the thresholds for EDT and ADDT scenarios are -98.2 dBm and 3.15, respectively. It can be observed from Fig. 18 that channel 45 is declared occupied by ADDT throughout the

TABLE VI
COMPARISON OF DIFFERENT INTERPOLATION SCHEMES

Channel	Method	p for IDW	Polynomial order	Optimal kernal function	Optimal Fitting Model	Optimal Nos of Neighbors	RMSE
45	IDW	1	NA	NA	NA	23	10.619
45	OK	NA	NA	NA	Exponential	43	10.423
45	UK	NA	Constant	Epanechnikov	Gaussian	23	10.509
46	IDW	1	NA	NA	NA	114	4.1
46	OK	NA	NA	NA	Circular	114	3.679
46	UK	NA	Third	Exponential	Gaussian	29	3.419
47	IDW	1	NA	NA	NA	114	1.947
47	OK	NA	NA	NA	Gaussian	97	1.824
47	UK	NA	Constant	Epanechnikov	Gaussian	5	1.812

measurement campaign while EDT misses to detect the PU signal in some regions. Similar results can be seen for channel 47 in Fig. 19. The better performance of the ADDT over EDT comes from the fact that the ADDT detector has better sensitivity as compared to the EDT detector. Note that the cyclostationary detector employed in this paper can detect the signal even at -107 dBm with more than 95% correct detection (see Fig. 7) while EDT cannot detect the signal if the RSSI falls below -98 dBm (approximately), which is the noise floor of the considered EDT detector (see Fig. 3).

Fig. 18 shows that the channel 45, which is classified as partially-occupied for our experiment, is being detected as fully occupied. Similarly, Fig. 19 shows that for channel 47, which is classified as free, detections are observed in few measurement locations. These observations are hardly surprising as the classification of the channels has been done based on the ability of the TSM-DVB-receiver to decode the signal on those channels while decisions regarding whether the region is occupied or unoccupied is based on the detection of the signal. Note that the detection of signal is possible for several dBs lower signal strength as compared to the minimum signal strength required for decoding the TV signal.

For the channel 47, it can be observed from Fig. 19 that EDT falsely declares the channel occupied around Espoo transmitter. This is a result of strong adjacent-channel-interference from channels 44 and 46 transmitted by Espoo transmitter. Although ADDT also gets affected by the strong adjacent-channel-interference as seen from Fig. 14(c), the effect is not as significant as for EDT. This can be seen from Fig. 19 where ADDT detects signals at few locations other than the Espoo transmitter. To corroborate the observations regarding strong adjacent-channel-interference, we also present results in Fig. 20 for channel 48, which was also classified as free based on the ability to decode the data with TSM-DVB receiver in the earlier measurement campaign. The nearest transmitter to Espoo on channel 48 is in Lohja (approximately 40 Km west of the measurement campaign) with following transmitter parameters: Latitude = 60.2667, Longitude = 24.1333, Mast height = 120 m, Transmission Power = 23.01 dB, and Transmitted Channels = 48, 55, 56, 60. It can be seen that while EDT again detects the signal around Espoo transmitter, ADDT correctly declares the channel unoccupied throughout the measurement region without getting significantly affected even by strong adjacent-channel-interference.

VI. CONCLUSION

In this paper, the performances of different spatial interpolation methods have been evaluated based on a large-scale measurement campaign using cyclostationary-based mobile sensors. Comparison of deterministic interpolation method of IDW and statistical interpolation methods of OK and UK has been carried out. It has been shown that Kriging schemes perform better than IDW. The performances of OK and UK methods are in same order. This is significant given that OK does not assume any information on trend and incurs lower computation complexity. Moreover, the performance of IDW and UK degrade if high number of neighboring measured points are included in the spatial interpolation at a given location.

Spatial interpolation results using cyclostationary test statistics have also been compared to the spatial interpolation results using energy-based test statistics. It has been shown that spatially estimated cyclostationary statistics suffer remarkably less from RF front-end nonlinearity than spatially estimated energy estimates. Thus, a field strength map with significantly higher sensitivity compared to energy estimates can be generated from the cyclostationary test statistics.

ACKNOWLEDGMENT

Authors would like to thank Dr. Jarmo Lundén for useful discussions.

REFERENCES

[1] I. Dagres and A. Polydoros, "Radio Environmental Maps: Information Models and Reference Model," FARAMIR, Tech. Rep., Apr. 2011. [Online]. Available: http://www.ict-faramir.eu/fileadmin/user_upload/deliverables/FARAMIR-D4.1-Final.pdf

[2] J. Oksanen, B. Kaufman, V. Koivunen, and H. V. Poor, "Robotics inspired opportunistic routing for cognitive radio using potential fields," *IEEE Transactions on Cognitive Communications and Networking*, vol. 1, no. 1, pp. 45–55, 2015.

[3] H. Hentila, J. Oksanen, and V. Koivunen, "Potential field based scheduling in cognitive radio networks," in *IEEE 17th International Workshop on Signal Processing Advances in Wireless Communications (SPAWC)*, 2016, pp. 1–6.

[4] R. Murthy, R. Chandra, T. Moscibroada, and P. Bahl, "Senseless: A Database-Driven Whitespaces Network," vol. 11, no. 2, Feb. 2012.

[5] R. Saeed and S. Shellhammer, *TV White Space Spectrum Technologies*. CRC Press, 2012.

[6] G. Boccolini, G. Hernandez-Penaloza, and B. Beferull-Lozano, "Wireless Sensor Network for Spectrum Cartography based on Kriging interpolation," in *23rd IEEE International Symposium on Personal Indoor and Mobile Radio Communications (PIMRC)*, Sept. 2012.

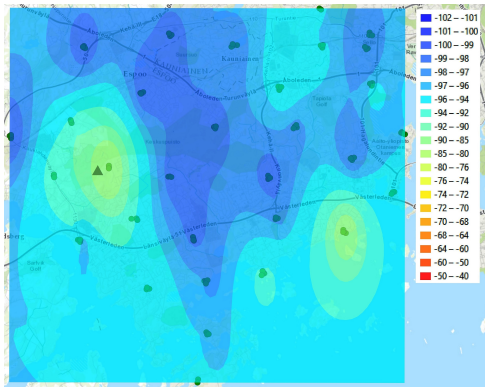

(a) Channel 45

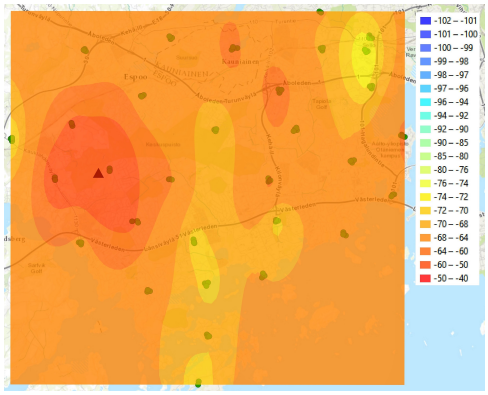

(b) Channel 46

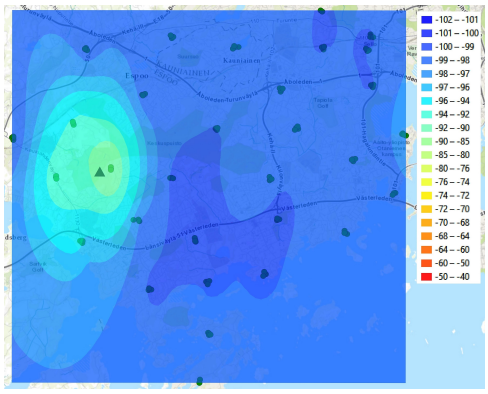

(c) Channel 47

Fig. 17. Spatial interpolation maps of EDT statistics for channels 45, 46, and 47 using exponential fit and OK. Note that the RSSI values shown in the labels are in dBm.

[7] S. Chaudhari, M. Kosunen, S. Mäkinen, J. Oksanen, M. Laatta, J. Ojaniemi, V. Koivunen, J. Ryynänen, and M. Valkama, "Performance Evaluation of Cyclostationary Based Cooperative Sensing Using Field Measurements," *IEEE Transactions on Vehicular Technology*, vol. 65, pp. 1982–1987, 2016.

[8] M. Kosunen, "Survey and analysis of cyclostationary signal detector implementations on FPGA," *IEEE Journal on Emerging and Selected Topics in Circuits and Systems*, vol. 3, no. 4, pp. 541–551, 2013.

[9] A. Ghasemi and E. Sousa, "Spectrum sensing in cognitive radio networks: requirements, challenges and design trade-offs," vol. 46, no. 4, pp. 32–39, Apr. 2008.

[10] V. Goncalves and S. Pollin, "The value of sensing for tv white spaces," in *IEEE International Symposium on Dynamic Spectrum Access Networks (DySPAN)*, 2011, pp. 231–241.

[11] A. Chakraborty and S. Das, "Measurement-augmented spectrum databases for white space spectrum proceedings," in *10th ACM International on Conference on emerging Networking Experiments and Technologies (CoNEXT)*, 2014, pp. 67–74.

[12] A. Achtzen, J. Riihijarvi, and P. Mahonen, "Improving accuracy for TVWS geolocation databases: Results from measurement-driven estimation approaches," in *IEEE International Symposium on Dynamic Spectrum Access Networks (DySPAN)*, 2014.

[13] F. Paisana, N. Marchetti, and L. A. DaSilva, "Radar, tv and cellular bands: Which spectrum access techniques for which bands?" vol. 16, no. 3, pp. 1193–1220, 2014.

[14] M. Umer, L. Kulik, and E. Tanin, "Spatial Interpolation in Wireless Sensor Networks: Localized Algorithms for Variogram Modeling and Kriging," *Geoinformatica*, vol. 14, pp. 101 – 134, 2010.

[15] P. Burrough and R. McDonnell, *Principles of Geographical Information Systems*. Oxford University Press, 1998.

[16] N. Cressie, *Statistics for Spatial Data*. John Wiley and Sons, Inc, 1993.

[17] S. Kim, E. DallAnese, and G. Giannakis, "Cooperative Spectrum Sensing for Cognitive Radios Using Kriged Kalman Filtering," *IEEE Journal of Selected Topics in Signal Processing*, vol. 5, no. 1, pp. 24–36, June 2010.

[18] R. Tandra and A. Sahai, "SNR walls for signal detection," *IEEE Journal of Selected Topics in Signal Processing*, vol. 2, no. 1, pp. 4 – 17, February 2008.

[19] L. Xing, "Comparison of reliability, delay and complexity for standalone cognitive radio spectrum sensing schemes," *IET Communications*, vol. 7, no. 9, pp. 799 – 807, 2013.

[20] T. Yucek, "A Survey of Spectrum Sensing Algorithms for Cognitive Radio Applications," in *IEEE Communications Surveys & Tutorials*, 2009, pp. 116–130.

[21] S. Chaudhari, M. Kosunen, S. Mäkinen, A. Cárdenas-González, V. Koivunen, J. Ryynänen, M. Laatta, and M. Valkama, "Measurement Campaign for Collaborative Sensing using Cyclostationary Based Mobile Sensors," in *IEEE International Symposium on Dynamic Spectrum Access Networks (DYSPAN)*, 2014, pp. 283 – 290.

[22] J. Lunden, V. Koivunen, A. Huttunen, and H. Poor, "Collaborative cyclostationary spectrum sensing for cognitive radio systems," *IEEE Trans. Signal Process.*, vol. 57, no. 11, pp. 4182–4195, 2009.

[23] S. Chaudhari, J. Lunden, and V. Koivunen, "Collaborative autocorrelation-based spectrum sensing of ofdm signals in cognitive radios," in *42nd Annual Conference on Information Sciences and Systems (CISS)*, March 2008, pp. 191–196.

[24] A. Dandawate and G. Giannakis, "Statistical Tests for Presence of Cyclostationarity," *IEEE Transactions on Signal Processing*, vol. 42, pp. 2355 – 2369, 1994.

[25] V. Turunen, "Correlation-Based Detection of OFDM Signals in the Angular Domain," *IEEE Transactions on Vehicular Technology*, vol. 61, no. 3, pp. 951–958, March 2012.

[26] S. Mäkinen, "Mobile spectrum sensing for cognitive radio," Master's thesis, Aalto University School of Electrical Engineering, 2014.

[27] T. Severini, *Elements of Distribution Theory*. Cambridge University Press, 2005.

[28] C. Geyer, "Lecture notes in stat 5101 notes: Brand name distributions," Jan. 2012.

[29] S. Kallionen, M. Vaarakangas, P. Hui, J. Ollikainen, I. Teikari, A. Parssinen, V. Turunen, M. Kosunen, and J. Ryynänen, "Multi-mode, multi-band spectrum sensor for cognitive radios embedded to a mobile phone," in *Cognitive radio oriented wireless network and communications*, 2011, pp. 236–240.

[30] R. Harjani, D. Cabric, D. Markovic, B. Sadler, A. Palani, R.and Saha, H. Shin, E. Rebeiz, S. Basir-Kazeruni, and Y. Fang-Li, "Wideband blind signal classification on a battery budget," vol. 53, p. 173 181, 2015.

[31] *TSM DVB T/H Diversity Test Receiver Manual*, Rohde and Schwarz. [Online]. Available: https://www.rohde-schwarz.com/us/manual/r-s-tsm-dvb-operating-manual-manuals-gb1_78701-29307.html?rusprivacypolicy=0

[32] P. Delfiner, *Geostatistics: Modeling Spatial Uncertainty, Volume 497*. John Wiley and Sons, Inc, 2009.

[33] J. Karl and B. Maurer, "Spatial dependency of predictions from image segmentation: a variogram-based method to determine appropriate scales for producing land-management information," vol. 5, pp. 194–202, Mar. 2010.

[34] B. Zhang and M. Stein, "Kernel Approximations for Universal Kriging Predictors," vol. 44, pp. 286–313, 1993.

[35] ArcGIS-Help. How kernel interpolation with barrier works? ArcGIS. [Online]. Available: https://desktop.arcgis.com/en/arcmap/10.3/guide-books/extensions/geostatistical-analyst/how-kernel-interpolation-with-barriers-works.htm

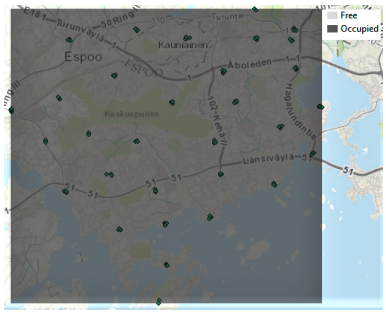

(a) ADDT

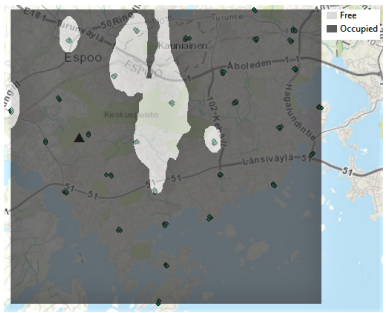

(b) EDT

Fig. 18. Performance comparison of EDT and ADDT detectors for channel 45.

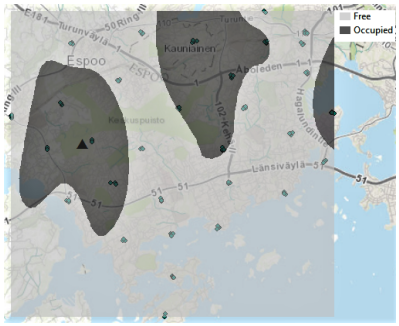

(a) ADDT

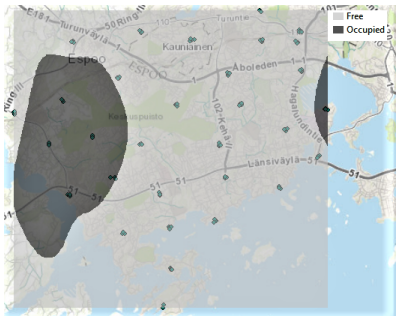

(b) EDT

Fig. 19. Performance comparison of EDT and ADDT detectors for channel 47.

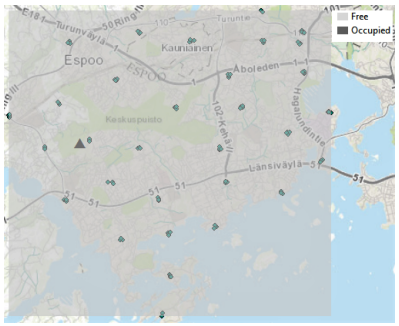

(a) ADDT

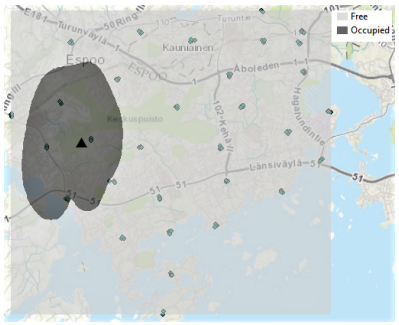

(b) EDT

Fig. 20. Performance comparison of EDT and ADDT detectors for channel 48.

[36] I. Rognoni, "Geostatistics in Cognitive Radios," Master's thesis, Politechico di Milano, Italy, Oct. 2014.
[37] C.Ramanathan, "Spatial Interpolation of Field Measurements for Cognitive Radio Networks," Master's thesis, Sastra University, India, Apr. 2016.
[38] ArcGIS. [Online]. Available: $https://www.arcgis.com/$. ArcGIS. [Online]. Available: https://www.arcgis.com/

Sachin Chaudhari (S'08, M'13) received his M.E. (Telecommunication) from Indian Institute of Science, Bangalore, India in 2004. From August 2004 to May 2007, he was with Esqube Communications, Bangalore, India as a senior wireless communication engineer. In June 2007, he joined the Department of Signal Processing and Acoustics at Aalto University (formerly TKK), Finland to pursue his PhD and received his D.Sc. (Tech) in 2012. During 2013-2014, he continued as a post-doctoral researcher at Aalto University. Since Dec. 2014, he is working as an Assistant Professor at the International Institute of Information Technology (IIIT), Hyderabad, India. His research interests are in the field of physical layer (PHY) signal processing for next generation wireless systems including 5G, cognitive radios, and internet of things (IoT).

Marko Kosunen (S'97-M'07) received his M.Sc., L.Sc., and D.Sc. (with honors) degrees from Helsinki University of Technology, Espoo, Finland, in 1998, 2001 and 2006, respectively. He is currently a Senior Researcher at Aalto University, Department of Micro and Nano Sciences. His expertise is in implementation of the wireless transceiver DSP algorithms and communication circuits. He is currently working on implementations of cognitive radio spectrum sensors, digital intensive transceiver circuits and medical sensor electronics.

Semu Mäkinen (M'15) was born in Joensuu, Finland in 1990. He reveived M.Sc degree in electrical engineering from Aalto University School of Electrical Engineering in 2015. During studies he worked as a research assistant for Laboratory of Circuit Design and did his master's thesis there. After graduation he worked for two years in a startup company, Enefix Electric Oy, where he was one of the founding members and responsible for the product design. In 2017 he joined Space Systems Finland where he currently works as a systems engineer.

C. Ramanathan is currently a Ph.D research scholar at Department of Electrical Engineering, IIT-Madras, Chennai. He studied B.Tech in Electronics and Communications Engineering at Sree Vidyanikethan Engineering College, Tirupati (affiliated to JNTU-Anantapur) in 2011. Between 2012-14, he was with Tata Consultancy Services as Systems Engineer. He received the M.Tech degree in Communication Systems from School of Electrical and Electronics Engineering, SASTRA University, Thanjavur, in 2016. He was an intern at IIIT-Hyderabad from Dec-2015 to May-2016 and completed his M.Tech thesis work under the guidance of Dr. Sachin Chaudhari. He was a receipient of Summer Research Fellowship from Indian Academy of Sciences during May 2015 to July-2015. He worked as Assistant Professor at Sree Vidyanikethan Engineering College, Tirupati, from Jun-2016 to Nov-2016, and as Research Project Officer in TeNeT group at Department of Electrical Engineering, IIT-Madras, Chennai, from Dec-2016 to Apr-2017. His research interests include Signal Processing for Wireless Communication, Cognitive Radio, Estimation and Detection Theory and their applications in the development of next generation wireless communication.

Jan Oksanen (S'10) received his M.Sc. with distinction in telecommunication engineering from the Helsinki University of Technology (currently known as Aalto University), Finland in 2008. He is currently finalizing his D.Sc. (Tech) at the department of Signal processing and acoustics, Aalto university and will defend his doctoral thesis in the near future. During Nov. 2011-Nov. 2012 he was a visiting student research collaborator at Princeton University, NJ, USA. His research interests include cognitive radio, spectrum sensing and machine learning.

Markus Laatta received his M.Sc. (Tech.) with distinction in electrical engineering from Tampere University of Technology (TUT), Finland, in 2017. During 20132014, he worked as a research assistant at the Department of Electronics and Communications Engineering at TUT. In 2013, he was working as a visiting researcher at the Department of Micro and Nano Sciences, Aalto University, Finland. He has also been working as a research assistant at TUT. He is currently working as an embedded system software designer at Wapice Ltd. His research interests include millimeter wave communication systems, beamforming techniques, cognitive radio, and embedded systems.

Visa Koivunen (M'87, SM'98, F'11) received the D.Sc. (Tech.) degree with honors from the Department of Electrical Engineering, University of Oulu, Oulu, Finland. He received the primus doctor (best graduate) award among the doctoral graduates in years 1989-1994. He is a member of Eta Kappa Nu. From 1992 to 1995 he was a visiting researcher at the University of Pennsylvania, Philadelphia, USA. Years 1997 -1999 he was faculty at Tampere UT. Since 1999 he has been a full Professor of Signal Processing at Aalto University (formerly known as Helsinki Univ of Technology) , Finland. He received the Academy professor position. He was one of the Principal Investigators in SMARAD Center of Excellence in Research nominated by the Academy of Finland. Years 2003-2006 he has been also adjunct full professor at the University of Pennsylvania, Philadelphia, USA. During his sabbatical term year 2007 he was a Visiting Fellow at Princeton University, NJ, USA. He has also been a part-time Visiting Fellow at Nokia Research Center (2006-2012). He spent a sabbatical at Princeton University for the full academic year 2013-2014.

Dr. Koivunens research interest include statistical, communications, sensor array and multichannel signal processing. He has published about 350 papers in international scientific conferences and journals. He co-authored the papers receiving the best paper award in IEEE PIMRC 2005, EUSIPCO2006,EUCAP (European Conference on Antennas and Propagation) 2006 and COCORA 2012. He has been awarded the IEEE Signal Processing Society best paper award for the year 2007 (with J. Eriksson). He served as an associate editor for IEEE Signal Processing Letters, IEEE Transactions on Signal Processing, Signal Processing and Journal of Wireless Communication and Networking. He is co-editor for IEEE JSTSP special issue on Smart Grids and a member of editorial board for IEEE Signal Processing Magazine. He has been a member of the IEEE SPS technical committees SPCOM-TC and SAM-TC. He was the general chair of the IEEE SPAWC conference 2007 conference in Helsinki, Finland June 2007. He is the the Technical Program Chair for the IEEE SPAWC 2015 as well as Array Processing track chair for 2014 Asilomar conference. He is the recipient of the EURASIP Technical Achievement Award in 2015.

Jussi Ryynänen (S'99-M'04) was born in Ilmajoki, Finland, in 1973. He received the M.Sc. and D.Sc. degrees in electrical engineering from the Helsinki University of Technology (HUT), Helsinki, Finland, in 1998, and 2004, respectively. He is currently a Professor in the Department of Micro- and Nanosciences, Aalto University School of Electrical Engineering. His main research interests are on integrated transceiver circuits for wireless applications. He has authored or coauthored over 100 refereed journal and conference papers in the areas of analog and RF circuit design. He holds several patents on RF circuits. Dr. Ryynnen is currently a member of the technical program committee of the IEEE International Solid-State Circuits Conference and IEEE European Solid-State Circuits Conference.

Mikko Valkama was born in Pirkkala, Finland, on November 27, 1975. He received the M.Sc. and Ph.D. Degrees (both with honors) in electrical engineering (EE) from Tampere University of Technology (TUT), Finland, in 2000 and 2001, respectively. In 2002, he received the Best Ph.D. Thesis award by the Finnish Academy of Science and Letters for his dissertation entitled "Advanced I/Q signal processing for wideband receivers: Models and algorithms". In 2003, he was working as a visiting researcher with the Communications Systems and Signal Processing Institute at SDSU, San Diego, CA. Currently, he is a Full Professor and Department Vice-Head at the Department of Electronics and Communications Engineering at TUT, Finland. His general research interests include communications signal processing, estimation and detection techniques, signal processing algorithms for software defined flexible radios, cognitive radio, full-duplex radio, radio localization, 5G mobile cellular radio, digital transmission techniques such as different variants of multicarrier modulation methods and OFDM, and radio resource management for ad-hoc and mobile networks.